Feng *et al. Journal of Nanobiotechnology* (2025) 23:145
https://doi.org/10.1186/s12951-025-03137-z

Journal of Nanobiotechnology

RESEARCH **Open Access**

Visualizing spatiotemporal pattern of vascularization by SWIR fluorescence imaging in a mouse model of perforator flap transplantation

Sijia Feng[1†], Mo Chen[2†], Huizhu Li[1†], Xiao Zhang[1], Xiner Du[1], Lu Fang[3,4], Kai Xu[1], Shunyao Li[1], Fuchun Chen[3,4], Yunxia Li[1], Fei Xiong[5], Dan Hu[6], Jingyi Mi[5*], Xuanfeng Qin[7*] and Jun Chen[1*]

Abstract

Vascularization as a spatiotemporally interlaced process involving angiogenesis and vascular remodeling, has seldom been investigated comprehensively regarding the interrelationship of the two intertwining but sequential processes. Here, a shortwave infrared (SWIR) fluorescence imaging strategy based on quantum dots (QDs) was designed to dynamically visualize vascularization in vivo and in situ in a perforator transplantation mouse model. The vascularization process could be directly perceived from the established flap model with an optimal observation window at 10 min post-injection. Anchored in SWIR technology and image processing, it was revealed that temporally, angiogenesis lasted throughout 21 days after surgery while vascular remodeling took a dominant role after 14 days both in vivo and in situ. Moreover, four perforasomes of the flap in situ displayed spatially that Zone IV shortened the vascularization process with sufficient blood supply from the LDCIA, while Zone II recovered slowly from ischemia with a lack of blood supply. This study serves as a pioneer in adding novel cognition to spatiotemporal pattern of vascularization through visualizing angiogenesis and vascular remodeling simultaneously and dynamically, thus facilitating further investigation into the mechanisms behind.

Keywords Angiogenesis, Vascular remodeling, In vivo imaging, SWIR, Flap

---

†Sijia Feng, Mo Chen and Huizhu Li have contributed equally to this work.

*Correspondence:
Jingyi Mi
mijingyi@suda.edu.cn
Xuanfeng Qin
qinxuanfeng777@163.com
Jun Chen
biochenjun@fudan.edu.cn
Full list of author information is available at the end of the article

Graphical Abstract

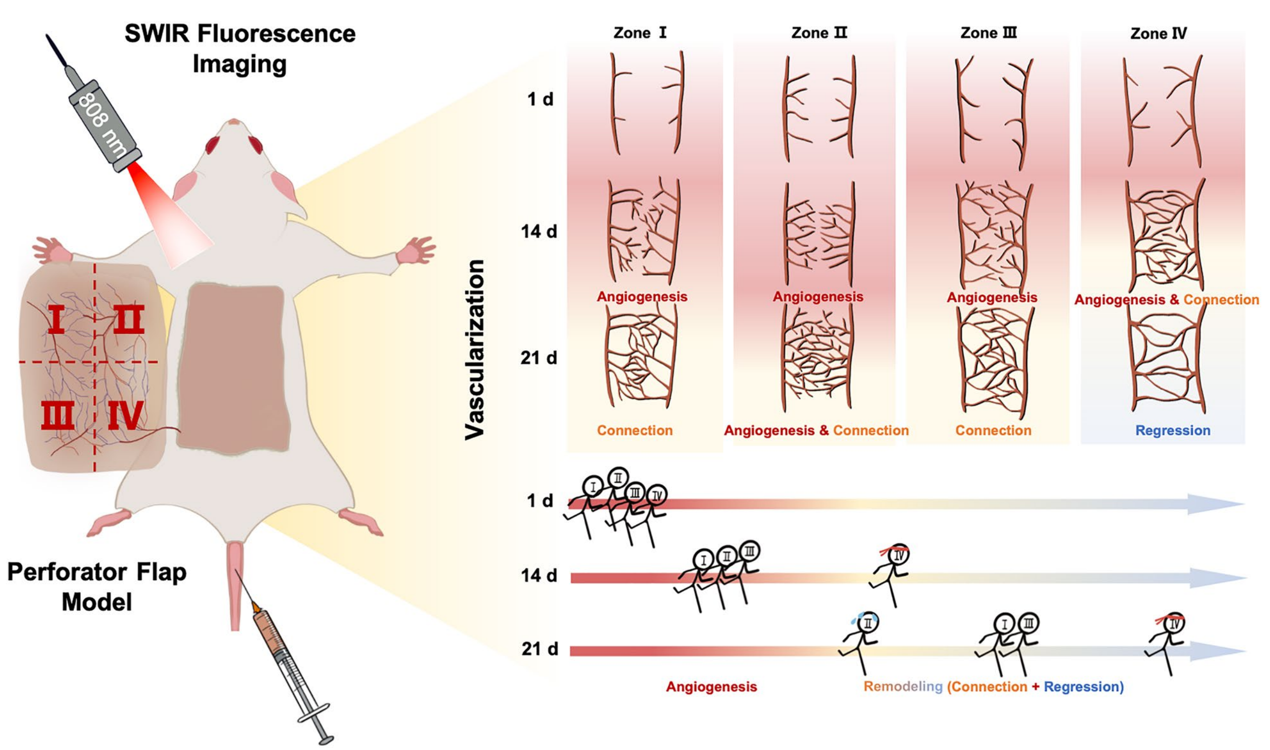

Introduction

The vascularization process includes angiogenesis characterized by forming new vessels from pre-existing vascular networks [1], in tandem with vascular remodeling, a transformation and maturation process involving vascular pruning, diameters adjusting, and establishment of vessel identity and hierarchy, which transforms the nascent vascular system into a functional network [2]. These two biological processes are pivotal for the construction and sustenance of a primary vascular system, not only facilitating the removal of metabolic waste, but also playing a critical role in nourishing tissues [3]. Most earlier studies focus on the two processes separately, studying angiogenesis as vessel splitting and sprouting [1, 2], as well as investigating vascular remodeling as varieties in vessel branching and connections [4, 5]. However, vascularization process is regarded as an interlaced process of both angiogenesis and vascular remodeling in space and time. Hence, it is imperative to conduct comprehensive investigation on the two components together as a dynamic, spatiotemporal and coordinated process, thus revealing in-depth insights into the mechanisms behind vascularization.

Recent advancements in imaging technologies make deciphering of the complex process of vascularization possible and feasible, because they allow for a more detailed and noninvasive examination of the vascular system [6]. Nonetheless, though the quest for an imaging technique that consistently mirrors the intricate spatiotemporal intertwining process including angiogenesis and vascular remodeling exists, current imaging strategies have not fully met the mark yet. Conventional imaging technologies that are predominantly utilized in monitoring and observation of blood vessels mainly include ultrasound, X-ray angiography, magnetic resonance angiography (MRA), and computed tomographic angiography (CTA). Despite their widespread use, these modalities are not without their drawbacks, such as radiation, limitations in spatial and temporal resolution, and restricted portrayal of dynamic information [7–11]. Notably, advanced imaging technologies for vascular system are also mushrooming. Superb microvascular imaging (SMI) acts as an advancing microvascular imaging in various medical disciplines [12]. Multimodal MRI and Micro-CT imaging can quantitatively assess the vascularization process [13]. Photoacoustic imaging technology enables deep tissue vascular imaging, aiding in the study of angiogenesis and the assessment of anti-angiogenic

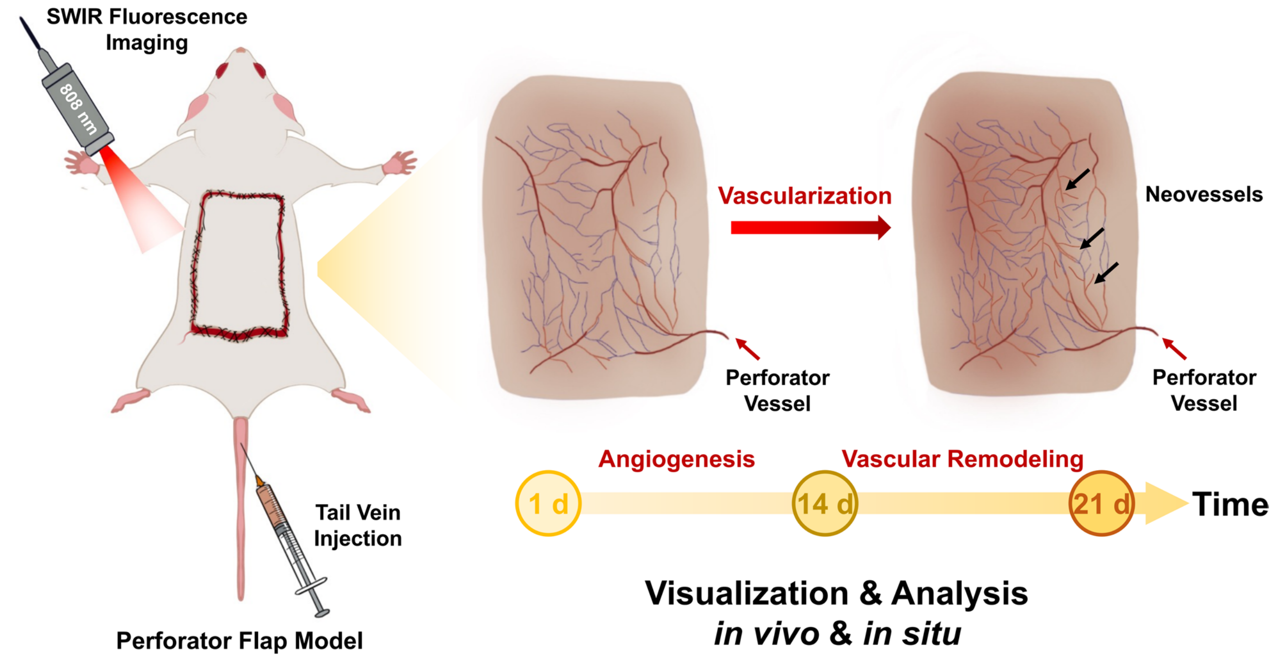

Scheme 1. Illustration of the vascularization process of the vessel network in a perforator flap transplantation mouse model visualized by SWIR fluorescence imaging

therapies [14]. While despite their effectiveness, the practical limitations of clinical deployment have limited their application in clinical practice. Most importantly, the above-mentioned imaging modalities are unable to capture the spatiotemporal properties of both angiogenesis and vascular remodeling simultaneously. Considering these limitations inherent to existing imaging approaches for vascularization analysis, there is a burgeoning interest in the development of novel imaging techniques with new strategies aiming to offer non-invasive, high-resolution, and exhaustive portrayals of the spatiotemporal characteristics of vascularization, especially dynamically monitoring the complicated interlaced process including angiogenesis and vascular remodeling, addressing the unmet needs of medical community in this specialized field.

The pioneering application of fluorescent angiography in the field of blood circulation, particularly for assessing blood flow within arterial and venous conduits, has been a tremendous progress. This technique visually captures the ingress and egress of blood, offering valuable insights into vascular dynamics [15]. With less photon absorption and scattering by tissues, the fluorescence imaging in the shortwave infrared (SWIR) window (1000–1700 nm) provides real-time information that probes deep into the body with increased spatial and temporal resolution [16]. Thus, SWIR fluorescence imaging has emerged as a prospective technique for in vivo bioimaging [17, 18]. For example, it has been applied for the in vivo imaging of intricate structures such as vascular system [19, 20]. Moreover, previous studies have confirmed that SWIR fluorescence imaging based on lead sulfide quantum dots (QDs) is capable of in vivo, real-time and long-time imaging of blood and lymphatic circulation [21–24]. On this basis, image processing techniques involving image-based analysis and quantification of vessel networks, have also played a pivotal role in analyzing the fluorescence images objectively and truthfully in these former studies. Therefore, in vivo SWIR fluorescence imaging combined with image processing techniques for robust, versatile and automated quantification of vascular network parameters, is considered as a promising candidate for conducting research on visualization of spatiotemporal pattern of vascularization by providing real-time, dynamic and objective data.

In this study, SWIR fluorescence imaging based on QDs was developed to capture the interlaced and dynamic process of angiogenesis and vascular remodeling, consistent with image processing for obtaining precise quantitative data, to illustrate the underlying mechanisms driving the observed vessel network development (Scheme 1). First, mice models of perforator flap transplantation were established, which were observed through a 21-day time course. Then, parameters of the flap were measured, and optimal observational window was decided, preparing for the following precise imaging. Afterwards, the flap in vivo and in situ were imaged using SWIR fluorescence imaging, respectively, and parameters including vessels area, diameter, length, number of vessel segments, junctions and endpoints were calculated to decode the spatiotemporal pattern of angiogenesis and vascular remodeling simultaneously. Finally, histological analysis was performed to verify the vascularization process. The significance of this study is highlighted by its potential to address critical spatiotemporal pattern during angiogenesis and vascular remodeling in a dynamic and synchronous way, contributing to the overall knowledge of vascular biology and unlocking the unprecedented therapeutic potential of vascular related diseases.

Methods

Preparation of QDs: QDs utilized in this study were synthesized according to the method described previously [24]. Briefly, 10 mM $Pb(CH_2COO)_2 \bullet 3H_2O$ and 50 mg/mL ribonuclease A (RNase A) from the bovine pancreas were mixed and the pH was adjusted to 9-10. Then 10 mM of Na_2S was added and the solution was put into the microwave immediately with the stir bar to heat at 70℃, 30W for 30 s. Afterwards, QDs were transferred to a 10 kDa ultrafiltration tube after cooling down and washed three times with PBS (pH = 7.4) (1500 rpm/min, 10 min) to remove the extra reagents and adjust the pH to 7-8. Finally, the as-prepared QDs were stored at 4 ℃ and utilized as a vessel contrast agent without further modification.

Animal Model: All the experimental animals were provided by the Shanghai Jiesijie Laboratory Animal Co, Ltd (6–8-week-old, ICR, female mice). Related animal studies were carried out in agreement with the guidelines approved by the Animal Care Committee of the Laboratory Animal from Fudan University. The establishment of the flap transplantation model was based on our previously reported method [22, 24]. The mice were anesthetized using isoflurane and placed in the prone position with depilation and disinfection of the surgical area on the back. A 4.5 cm × 2.5 cm dorsal island perforator skin flap was established. The left deep circumflex iliac artery (LDCIA) perforator was preserved as a pedicle while the other main perforators including right deep circumflex iliac artery (RDCIA) perforator, right lateral thoracic artery (RLTA) perforator, left lateral thoracic artery (LLTA) perforator were disconnected when the flap was overturned in situ. Then the flap was sutured back using a 6-0 nylon.

SWIR fluorescence imaging and analysis The SWIR fluorescence videos and images were obtained with MARS (Artemis Intelligent Imaging, Shanghai, China) with 808 nm excitation and 1250 nm NIR long-pass filter. SWIR fluorescence videos and images were taken 1 d, 14 d and 21 d after establishment of the flap transplantation model (n = 3 at each time point). For each time point, in vivo and in situ videos were taken respectively, and elevation of the flap was conducted only once for each animal to minimize the impact of surgery. The flap areas in the videos were selected with other parts clipped, and then the videos were accelerated to ten times. The area, maximum length and maximum width of the whole flap in vivo and in situ were both measured in gross. Then, the mice models were intravenously injected with 0.35 mL QDs for imaging. After imaging, parameters of the four perforators and the flap vessel network were measured with the flaps dissected and turned over from the left in the prone position, including 1) vessel diameter: PL intensity of a line perpendicular to a single perforator was measured from fluorescence images with ImageJ and full width at half maximum (FWHM) of Gaussian fitting was calculated as the vessel diameter using Origin; 2) vessels length, vessels area, percentage vessels area, number of segments, junctions and endpoints: images were preprocessed with Frangi filtering to enhance the tubular structures and the images (8-bit) were imported to AngioTool [25] to obtain these parameters; 3) PL intensity of the four perforator vessels from the origin to the end: a line was drawn from the origin (peripheral region) of the perforator to the end (central region) with a length of 25 pixels and the PL intensity along this line was measured.

Histology and quantitative analysis The flap tissue was collected at 1 d, 14 d and 21 d after establishment of the flap transplantation model for the Hematoxylin and Eosin (H&E) staining and immunohistochemistry. The tissues were placed in 4% paraformaldehyde before paraffin embedding. 4 μm cross-sections were deparaffinized and rehydrated for immunohistochemistry. Then they were immersed in sodium citrate antigen retrieval solution, blocked in 3% H_2O_2, covered with 10% normal rabbit serum at room temperature for 30 min, and incubated overnight with Anti-CD31 antibody (ab182981, Abcam), Anti-vascular endothelial growth factor (VEGFA) antibody (EP1176Y, Abcam), Anti-von Willebrand factor (VWF) antibody (11778-1-AP, Proteintech), and α-smooth muscle actin (α-SMA, 14395-1-AP, Proteintech) followed by secondary antibody (Servicebio, GB23303). Epidermal thickness, dermal thickness and fibroblast proliferation were measured from the H&E micrographs. The thickness was measured from 5 different points from each slide. Vessel number was measured from the CD31 stained immunohistochemical micrographs. It was analyzed at a magnification of × 200 and average number of the vessels from three different visual

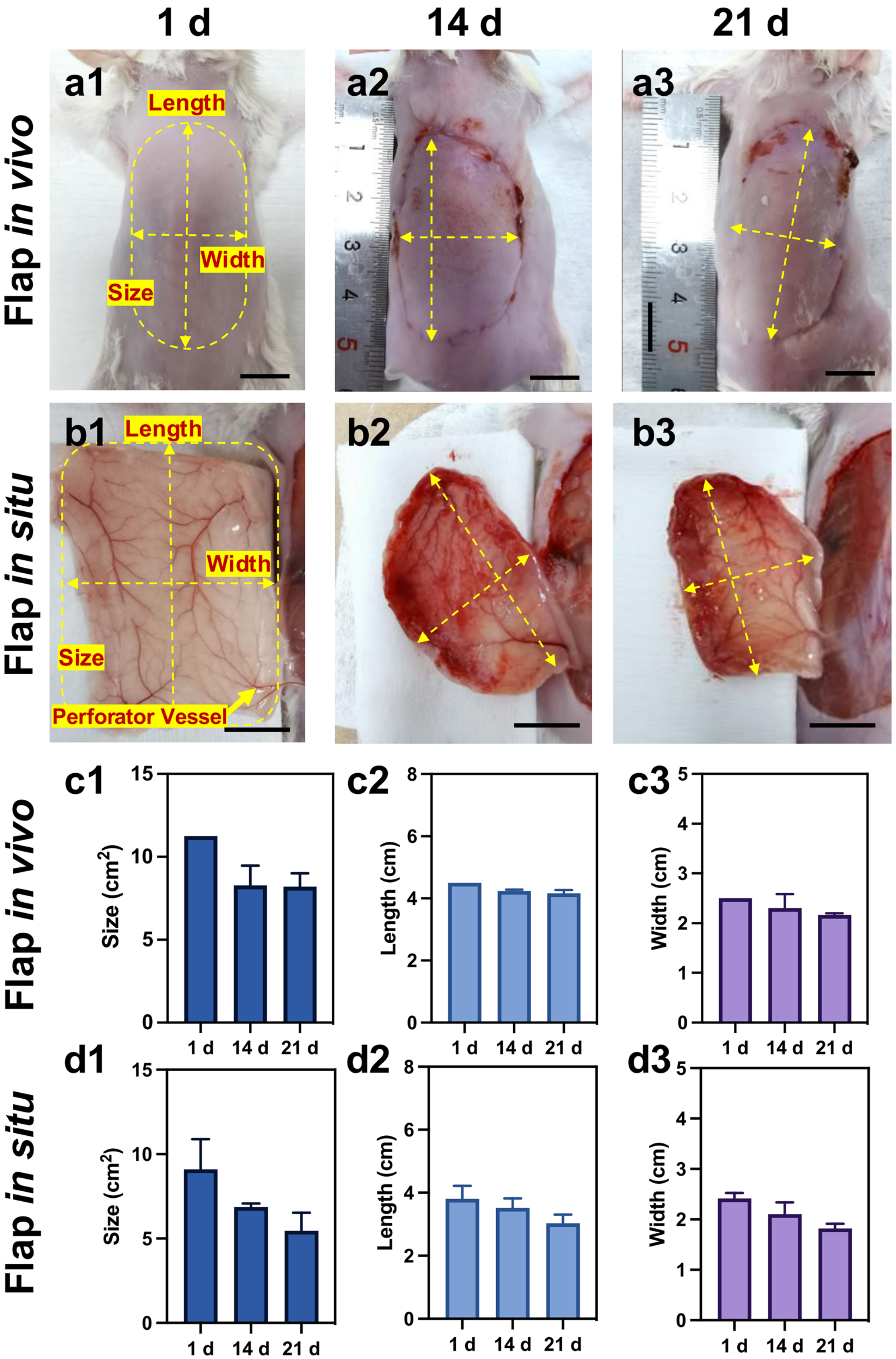

Fig. 1 The shape and size variation of flap in vivo and in situ in a time course. **a1**–**a3** Observation of the flap in vivo and **b1**–**b3** in situ at 1 d, 14 d and 21 d. **c1**–**c3** The size, length and width of the flap in vivo measured from **a1**–**a3**). **d1**–**d3** The size, length and width of the flap in situ measured from **b1**–**b3**. Scale bar: 1 cm

fields of slices were calculated. Mean density of CD31, VEGF, VWF and α-SMA measured from immunohistochemical micrographs. Mean density was calculated by integrated optical density divided by positive pixel area, which were measured with ImageJ.

Statistical analysis All the data from experimental animals (n = 3 at each time point) were included in the statistical analysis. The comparisons were performed and analyzed using GraphPad Prism 8.0. Ordinary one-way ANOVA test was performed for the comparison and P value < 0.05 was considered statistically significant with *; < 0.01 with **; < 0.001 with ***.

Results and discussions

After the establishment of mice models with perforator flap transplantation (Additional file 1: Figure S1), the bright field photographs of the flap in vivo and in situ were captured at 1 d, 14 d and 21 d post-surgery, respectively. Specifically, the flap was dissected at 1 d (Fig. 1a1) and turned over (Fig. 1b1) with the perforator vessel preserved to maintain blood supply from the body. Then, the flap was sutured back after SWIR fluorescence imaging and turned overrespectively at 14 d (Fig. 1a2-a3) and 21 d (Fig. 1b2-b3) for imaging. During the longitudinal observation, it was discovered that compared with the originally dissected flap at 1 d, the shape of the flap varied from a rectangle to an oval at 14 d and 21 d by direct observation. Moreover, the size, length and width of the flap in vivo (Fig. 1c1-c3) and in situ (Fig. 1d1-d3) were measured respectively from the photographs. The quantitative measurement showed that the flap size decreased from 1 d to 21 d both in vivo and in situ, in consistent with the direct observation. Then, the detailed analysis demonstrated that both the length and width of the flap shortened constantly from 1 d to 21 d, contributing to the decrease in flap size jointly.

The current results indicated no necrosis but the occurrence of contracture of the flap throughout 21 days. It is documented that the flap undergoes contracture during the vascularization process, facilitating wound healing [26]. Consequently, it could be deduced that vascularization occurred and led to the morphologic changes of the flap, which was clearly and visually displayed by this flap transplantation model. To delve into the spatiotemporal variation during vascularization beyond the appearances, an imaging strategy was in urgent need to realize visualizing vascularization dynamically as well as evaluating the process accurately based on the present flap model.

Exhibiting excellent properties of high penetration depth and low autofluorescence, SWIR fluorescence imaging based on QDs was chosen as the candidate for obtaining high-resolution and real-time data in this study. The schematic illustration depicted the four perforator vessels of the dissected flap in Fig. 2a, and the bright field photograph was displayed as a reference for the following SWIR fluorescence images (Fig. 2b). Videos were recorded after intravenous injection of the QDs through tail vein in a mouse model of perforator flap transplantation, from the beginning of injection till the disappearance of fluorescence signals (clipped as Additional file 2: Movie S1 and Movie S2). Continuous images were captured based on the videos (Fig. 2c1-c10). As shown in Fig. 2c1, the preserved perforator LDCIA lighted up immediately after injection and its branches and choke vessels were rapidly imaged within 1 s in quick succession. Then, the LLTA was detected straightly from blood flow of the LDCIA from 5 s to 30 s post-injection (Fig. 2c2-c4). After that, the branches of the LLTA as well as the RDCIA and its branches could be visualized from 60 s to 5 min post-injection (Fig. 2c5-c6). Finally, the latest imaged perforator RLTA and its branches could be observed around 10 min post-injection (Fig. 2c7), which was also regarded as the time point of successful imaging of the whole flap vessels through SWIR technology. Gradually, the fluorescence signals detected from the flap vessels faded away and lasted till 70 min post-injection, due to the metabolism and outflow of the QDs in the circulation (Fig. 2c8-c10). This result not only demonstrated a detailed and specific map of vascular system in a perforator flap model, but also uncovered a sequential variation of blood flow among flap vessels especially the four perforators, paving the way for in-depth decoding the spatiotemporal pattern of flap vascularization.

To further investigate the optimal time window for flap vessels imaging and observation based on SWIR technology, PL intensity and percentage area of the QDs-perfused flap were measured and calculated based on the obtained SWIR fluorescence images. From 10 s to 10 min post-injection, the PL intensity stayed at a high level and gradually decreased from 10 min to 70 min post-injection

(See figure on next page.)

Fig. 2 SWIR fluorescence imaging of the flap in situ immediately after QDs injection. **a** Schematic illustration and **b** bright field photograph of four perforator vessels of the dissected flap. **c1**–**c10** SWIR fluorescence images of the flap in situ at 1 s, 5 s, 10 s, 30 s, 60 s, 5 min, 10 min, 15 min, 45 min and 70 min after QDs injection. **d** PL intensity and **e** percentage area measured from **c1**–**c10**. **f** Combined graph of **d** and **e**) with optimal observation window marked. LDCIA: left deep circumflex iliac artery, LLTA: left lateral thoracic artery, RDCIA: right deep circumflex iliac artery, RLTA: right lateral thoracic artery. Scale bar: 0.5 cm

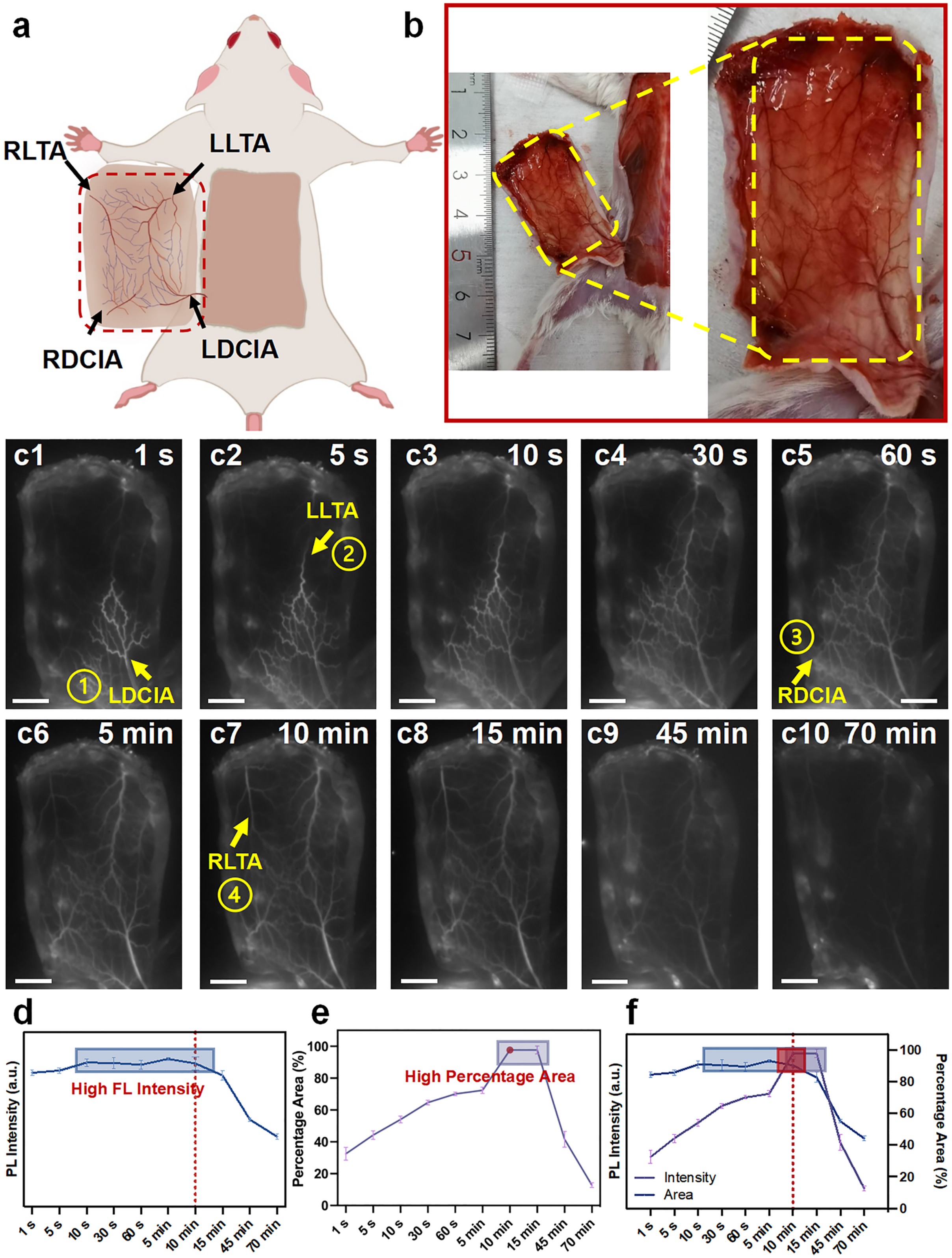

Fig. 2 (See legend on previous page.)

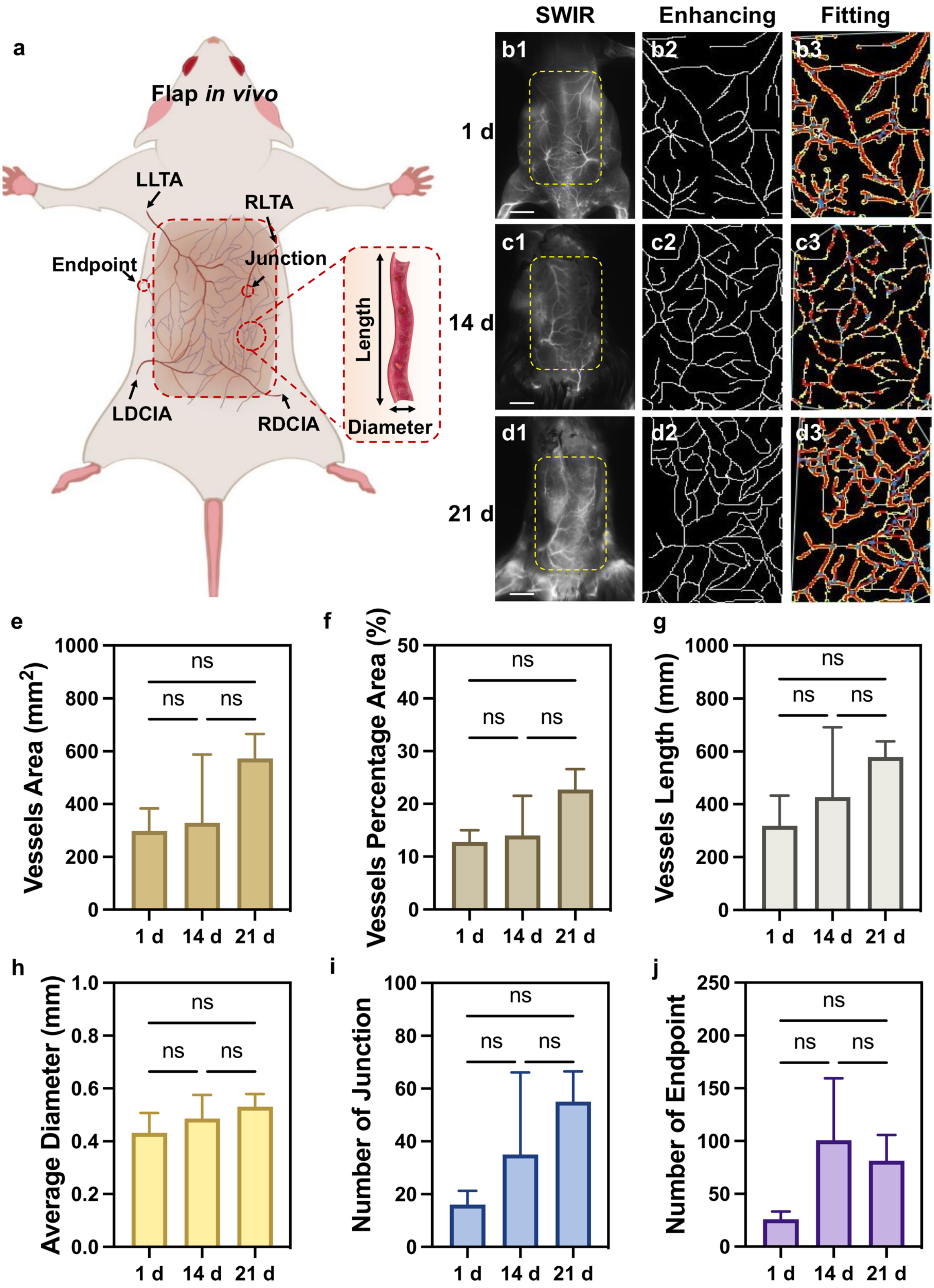

Fig. 3 Vessel analysis of the flap in vivo based on SWIR fluorescence imaging. **a** Schematic diagram of parameters measured on the flap in vivo. **b1**–**d1** Original SWIR fluorescence images, **b2**–**d2** enhanced images and **b3**–**d3** fitted images at 1 d, 14 d and 21 d post-surgery. **e** Vessels area, **f** vessels percentage area, **g** total vessels length, **h** average diameter of the four perforator vessels, **i** number of junctions and **j** number of endpoints of the flap measured from processed images. Scale bar: 1 cm

(Fig. 2d). Meanwhile, the percentage area gradually increased from 1 s to 10 min post-injection and shaped a peak at 10 min to 15 min post-injection, then decreasing to an undetectable level (Fig. 2e). Therefore, it was suggested that besides still images depicting the vascular system, dynamic recording of the blood flow pattern of the flap could be further achieved by SWIR fluorescence imaging. Furthermore, the optimal time window for the flap vessels observation was deciphered as around 10 min post-injection, regarding the intersection of both high PL intensity and percentage area (Fig. 2f). On this basis, 10 min post-injection was selected as the time point to acquire images each time after injection of QDs at 1 d, 14 d and 21 d post-surgery in the subsequent observation, assuring the comparability and standardization of the image acquirement in the current study.

To further decipher the spatiotemporal pattern of vascularization in a flap (Fig. 3a), the flap before dissection at 1 d (Fig. 3b1), 14 d (Fig. 3 c1) and 21 d (Fig. 3d1) post-surgery was analyzed in vivo using SWIR fluorescence imaging. Enhanced (Fig. 3b2-d2) and fitted images (Fig. 3b3-d3) were simultaneously acquired through image processing. Then, vessels area (Fig. 3e), vessels percentage area (Fig. 3f), total vessels length (Fig. 3g), average diameter of the four perforator vessels (Fig. 3h), number of vessel junctions (Fig. 3i) and endpoints (Fig. 3j) in the vascular system of the flap were measured from the fitted images. However, although vessels area, vessels percentage area, average vessel diameter, total vessels length and number of vessel junctions all demonstrated a gradually increasing trend in a time course, no statistical significance was shown. It was suggested that when the dissected flap was sutured back, the vessels reacted positively to the ischemic microenvironment to maintain perfusion (Fig. 3e–i). As a result, the area of vessels enlarged, vessel diameter and length both increased, as well as sprouting of neovessels indicated by increase of vessel junctions, was also activated to initiate angiogenesis. Furthermore, PL intensity of the four perforator vessels was measured from the origin to the end (Additional file 1: Figure S2). From 1 d to 21 d post-surgery, the PL intensity increased from the origin to the end in RLTA, LLTA, RDCIA and LDCIA, indicating an increase of perfusion from peripheral region to the central region of the flap. These results were consistent with the previously reported studies that angiogenesis involved constructing a new vascular network after surgery, which was the key to improving the blood supply and maintaining viability of the flap [27–29].

Notably, the vessel endpoints showed a different trend that increased at 14 d, while fell back at 21 d (Fig. 3j), seemingly contrary to the constantly elevating vascularization level and vascular remodeling. To be noted, it is acknowledged that postoperative vascularization presents as a complicated spatiotemporal process [30], encompassing angiogenesis mainly including neovessel formation marked by increasing endpoints and vascular remodeling involving alterations in vessel diameter and junctions.[27]. Currently, the endpoints indicating the free ends of blood vessels, was indicated to connect with each other to form vascular circuits during vascular remodeling, as a strategy to promote neovessel-network maturation and organization [30]. Therefore, the decrease of vessel endpoints could be decoded as the enhancement of vascular remodeling after angiogenesis.

To sum up, based on SWIR fluorescence imaging, not only the angiogenesis process increasing with time from 1 d to 21 d post-surgery was visualized, but also the vascular remodeling process enhancing after 14 d post-surgery was unveiled in vivo, contributing to profound understanding of vascularization sequentially from in vivo level. However, the fluorescence signals from the inner organs might interfere with that from the flap when observed in vivo. Therefore, a superiorly accurate approach of visualization was necessary for highly precise results.

To obtain a more accurate analysis and quantify the temporal pattern of vascularization excluding the inherent interference, the dissected flap was imaged in situ at 1 d, 14 d and 21 d post-surgery. Parameters including vessels area, length, diameter, as well as vessel segments, junctions and endpoints in the dissected flap were measured and compared utilizing SWIR fluorescence imaging (Fig. 4a). The SWIR fluorescence images of the flap in situ at 1 d, 14 d and 21 d post-surgery were demonstrated in Fig. 4b1-d1, along with enhanced (Fig. 4b2-d2) and fitted images (Fig. 4b3-d3), respectively. After image processing, the enhanced images could sharpen the vessel

(See figure on next page.)

Fig. 4 Vessel analysis of the flap in situ based on SWIR fluorescence imaging. **a** Schematic diagram of parameters measured from the flap in situ. **b1**–**d1** Original SWIR fluorescence images, **b2**–**d2** enhanced images and **b3**–**d3** fitted images at 1 d, 14 d and 21 d post-surgery. **e** Vessels area, **f** vessels percentage area, **g** total vessels length, **h** average diameter of the four perforator vessels, **i** number of vessel segments, **j** total vessel length/number of vessel segments of the flap measured from processed images. **k** Schematic illustration of number of junctions and endpoints during angiogenesis and connection. **l** Number of junctions and **m** number of endpoints of the flap measured from processed images. Scale bar: 0.5 cm

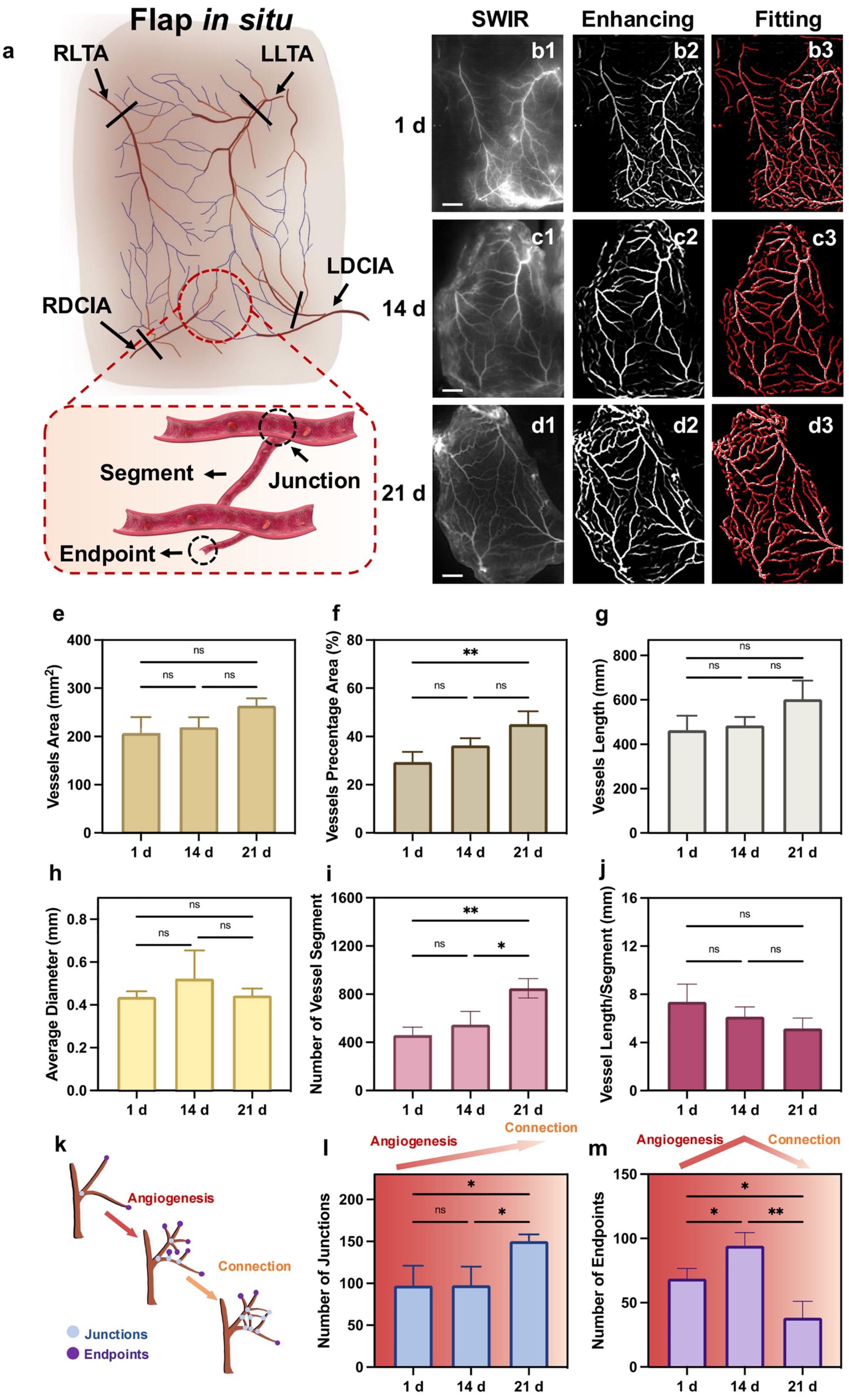

Fig. 4 (See legend on previous page.)

outline, thus enabling clear recognition of vessel details, while the fitted images were analyzed by software to provide standardized and accurate quantitative data.

For general evaluation, although an increase of vessels area was shown from 1 d to 21 d, no significant difference was discerned throughout the period of observation (Fig. 4e). To demonstrate the perfusion area more accurately, the vessels percentage area was calculated by excluding the impact of contracted flap size (Fig. 4f). A constant increase from 1 d to 21 d was displayed, along with a significant increase between 1 d and 21 d, indicating an increased perfusion after surgery. This result illustrated the same perfusion trend compared the in vivo data, again confirmed the increased vascularization activated by surgery, in accordance with studies reporting that increased vascular density could result in the improved blood flow, thus contributing to the survival of the flap [31, 32]. Consistent with vessels area and percentage area, a steady rise of the total vessels length from 1 d to 21 d was demonstrated though without significance (Fig. 4g), suggesting the persistent occurrence of angiogenesis process manifested by increase of vessel number throughout 21 days after surgery. Further, the average diameter of the four perforator vessels was measured to identify the changes of vessels responsible for major blood supply of the flap (Fig. 4h). It was shown that the vessel diameter increased from 1 d, and then decreased at 21 d but without significant difference. However, the trend indicated that after 14 d when the flap obtained sufficient perfusion, less blood supply might be enough overtime, resulting in reduced diameter as a manifestation of vascular remodeling process. In accordance with the present results, previous studies also demonstrated that the diameters of vessel began to expand immediately after surgery, and in the following days, some of them continues to expand while others gradually dwindled [28, 33, 34].

As for more detailed aspects of the configuration of the vessels, the number of vessel segments exhibited a significant increase from 1 d to 21 d (Fig. 4i). While the vessel length/segment constantly decreased throughout time, though no significance was revealed (Fig. 4j). Additionally, the vessel junctions demonstrated a significant increase in number from 1 d to 21 d (Fig. 4l). Referring to illustration Fig. 4k, the combined results implied that angiogenesis embodied by sprouting to form segments and junctions appeared continuously during the 21-day period. These findings agreed with prior studies, noting that the vascular network undergo the angiogenesis for expansion marked by sprouting and further formation of branches [5, 35, 36]. Interestingly, although significantly more endpoints were identified from 1 d to 14 d, a significant reduction of number was followed from 14 d to 21 d (Fig. 4m). Similar to the results of flap in vivo, the decrease in vessel endpoints considered to suggest the connection of branches appeared in flap in situ as well, revealing the active vascular remodeling process from 14 d to 21 d. This novel result corroborated the earlier findings that the sprouted vessels would eventually anastomose to form vascular loops and then vessel connectivity would be rearranged [1, 5, 36].

In conclusion, the flap vessel vascularization followed an interacted but sequential pattern, which was visualized by SWIR technology dynamically and in real-time. On one hand, angiogenesis existed and increased constantly during the 21-day period after surgery, resulting in increased vessels area and length in general as well as more segments and junctions in detail. On the other hand, vascular remodeling exercised its dominance mainly from 14 d to 21 d at the later stage of the vascularization, inducing perforator vessel diameter shrinkage and connection of vessel endpoints. Thus, the temporal trend of vascularization was visualized and quantified via SWIR technology, depicting the first half of the spatiotemporal pattern of vascularization.

To complete the other half of the puzzle, the flap in situ was spatially divided into four zones called perforasomes based on blood supply from the four perforator vessels [34, 37] (Fig. 5a). Aiming for the evaluation of spatiotemporal changes of vessels in each perforasome, the SWIR fluorescence images were acquired first, and the images were processed and analyzed in detail at 1 d, 14 d and 21 d post-surgery (Fig. 5b). Then, quantification analysis was conducted accordingly regarding the vessels percentage area as well as the number of vessel junctions and endpoints in the four flap zones, which were the major parameters that showed significance in the whole flap assessment in Fig. 4.

A significant increase in vessels percentage area from 1 d to 21 d post-surgery was illustrated in Zone I and

(See figure on next page.)

Fig. 5 Vessel analysis of the four perforasomes of the flap in situ based on SWIR fluorescence imaging. **a** Schematic diagram of the four perforasomes (divided into four zones) of the flap in situ. **b** SWIR fluorescence images of the four flap zones at 1 d, 14 d and 21 d post-surgery. **c1**–**c4** Vessels percentage area of the four flap zones. **d1**–**d4** Number of junctions and endpoints of the four flap zones. **e** Schematic illustration of the spatiotemporal patterns of vascularization in the four flap zones throughout 21 days. RLTA: right lateral thoracic artery, LLTA: left lateral thoracic artery, RDCIA: right deep circumflex iliac artery, LDCIA: left deep circumflex iliac artery. Scale bar: 0.5 cm

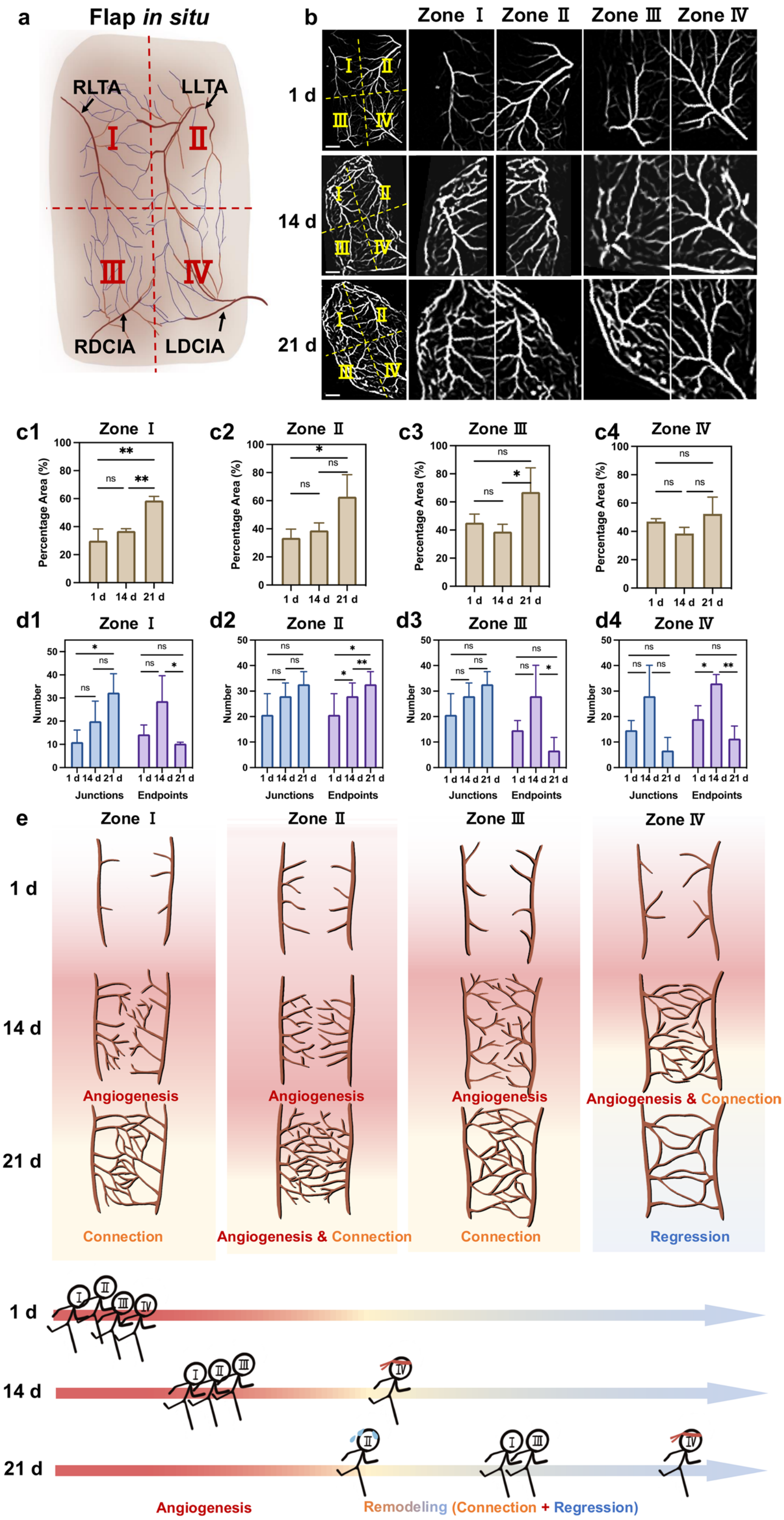

Fig. 5 (See legend on previous page.)

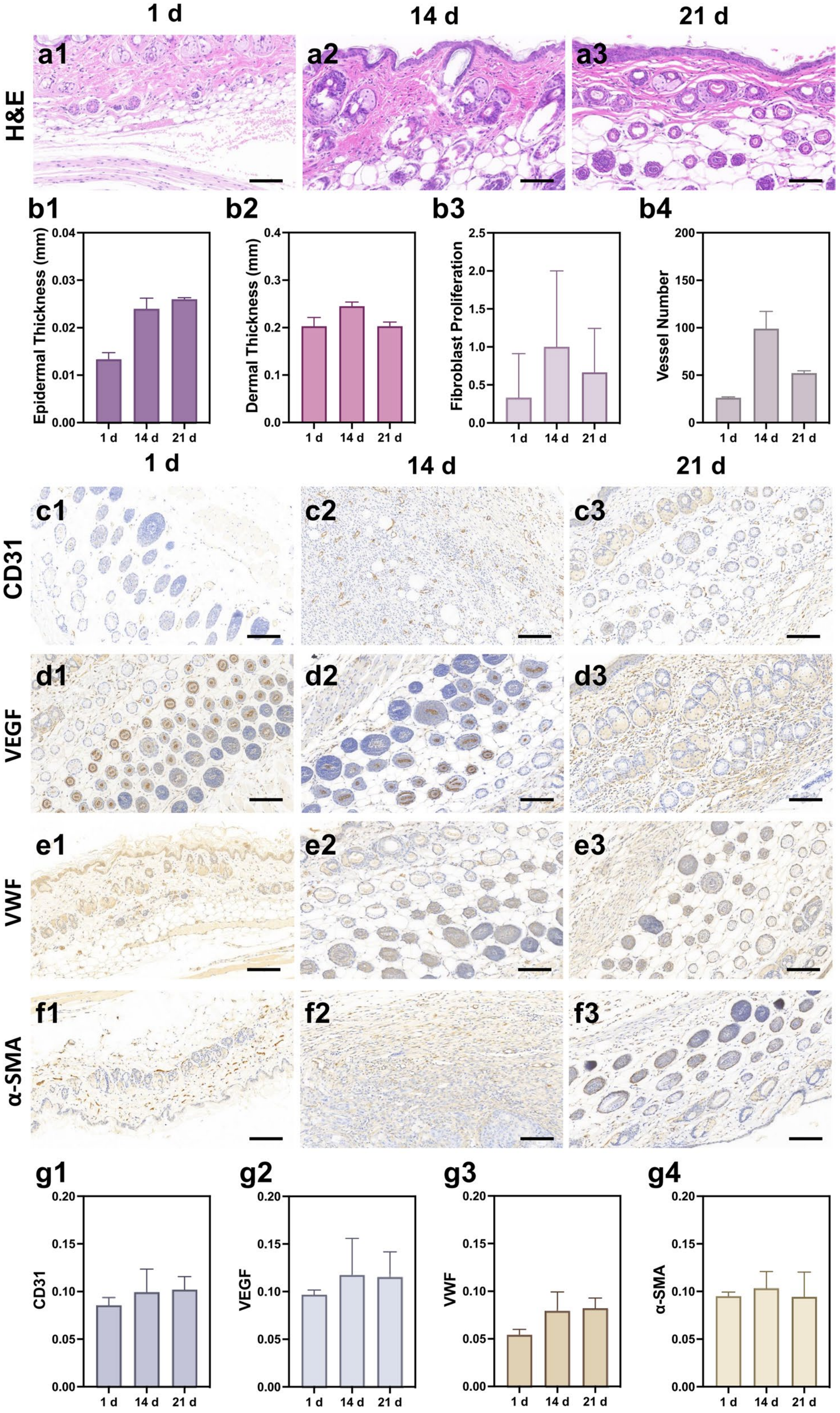

Fig. 6 Histological analysis of the flap. **a1**–**a3** Representative H&E staining micrographs (scale bar: 50 μm). **b1** Epidermal thickness, **b2** dermal thickness, **b3** fibroblast proliferation and **b4** vessel number measured form the H&E staining micrographs. **c1**–**c3** CD31, **d1–d3** VEGF, **e1**–**e3)** VWF and **f1**–**f3** α-SMA stained immunohistochemical micrographs (Scale bar: 100 μm) of the flap. **g1–g4** Mean density of CD31, VEGF, VWF and α-SMA measured from immunohistochemical micrographs

Zone II (Fig. 5c1-c2), and from 14 d to 21 d post-surgery in Zone III (Fig. 5c3), which implied an active angiogenesis process in these three zones overtime when facing ischemia. On the contrary, the vessels percentage area showed no significant changes in Zone IV during the 21-day period (Fig. 5c4). This result was in accordance with the fact that the perforator vessel in Zone IV (LDCIA) was the only perforator that was preserved to connect to the body circulation when establishing the flap model. In addition, the average vessel diameter and total vessel length were also measured, but no significance was demonstrated (Additional file 1: Figure S3). Hence, it could be suggested that when the flap was in a relatively ischemic state, the area supplied by the preserved perforator had relatively adequate perfusion, while other area might face greater risk of ischemia thus inducing more intense angiogenesis.

Most importantly, it was unfolded that not only a spatial map of vascular distribution and extension was identified, but a timeline charted with turning point of a sequential progression of vascularization process was also deciphered. As shown in Fig. 5d1–d3, a continuous increasing trend of vessel junctions was revealed in Zone I, Zone II and Zone III from 1 d to 21 d post-surgery, indicating a sustaining angiogenesis process. As for vessel endpoints, Zone I and Zone III showed similar trend in which a peak occurred at 14 d then followed by a decrease at 21 d post-surgery, while the number increased continually in Zone II. As previously mentioned, angiogenesis and vascular remodeling are two interacted but sequential process during vascularization. Thereby, it could be inferred that although Zone I, Zone II and Zone III initiated active angiogenesis immediately after surgery, Zone I and Zone III entered vascular remodeling phase with formation of connections earlier than Zone II at 14 d post-surgery. Meanwhile, it was suggested that Zone II might experience delayed angiogenesis and vessel remodeling.

Concerning Zone IV (Fig. 5d4), both the vessel junctions and endpoints in this area demonstrated a peak of number at 14 d post-surgery and fell back at 21 d. This pattern could be understood that the neovessels formed during the angiogenesis process were partially pruned (known as a part of vascular remodeling) during 14 d to 21 d, triggering a decrease of vessel junctions. Besides, vascular remodeling accelerated to form vascular connections synchronously, contributing to a reduction of vessel endpoints. It could be because Zone IV was endowed with relatively sufficient blood supply via LDCIA, vessels in this area experienced angiogenesis process fast and then vascular remodeling process, and firstly entered vascular regression process (a key developmental process occurring during late vascular remodeling) in which select capillaries were removed [1, 2].

In short, from the perspective of spatial distribution, Zone IV supplied by the only preserved perforator vessel featured comparatively more perfusion than the other three zones. More importantly, as the illustration Fig. 5e which decoded from the spatiotemporal pattern of vascularization captured by SWIR fluorescence imaging, vessels in Zone IV entered and advanced in the vascularization process more rapidly than the vessels in the Zone I and Zone III. While vessels in Zone II was perceived as the last of the four zones in the progression of vascularization.

To verify the occurrence of vascularization in the flap model, H&E staining (Fig. 6a1-a3) and immunohistochemical staining of angiogenesis markers including CD31 (Fig. 6c1-c3), VEGF (Fig. 6d1–d3), VWF (Fig. 6e1-e3) and α-SMA (Fig. 6f1-f3) were performed and quantified at 1 d, 14 d and 21 d post-surgery. Epidermal thickness (Fig. 6b1), dermal thickness (Fig. 6b2), fibroblast proliferation (Fig. 6b3) and vessel number (Fig. 6b4) measured form H&E staining showed increase at 14 d and the last three fell back at 21 d, indicating the recovery of flap at 21 d. According to Fig. 6g1-g4, mean density of CD31, VEGF, VWF and α-SMA increased gradually from 1 d to 14 d, with a slight increase or decrease at 21 d post-surgery. The results confirmed the vascularization along with steadily increasing vessel markers in a time course. Finally, biosafety of the QDs was examined. Major organs of the mice with injection of QD were harvest at 21 d post-injection, including the lung, heart, spleen, kidney and liver (Additional file 1: Figure S4). No obvious abnormality was observed in appearance. Compared with the control group, the H&E staining of the tissues showed no noticeable injury or inflammation, which ensuring the biosafety of QDs injection.

Conclusion

In this study, the spatiotemporal pattern of vascularization was visualized in a perforator flap transplantation mouse model utilizing SWIR fluorescence imaging. First, the flap in situ model was considered more suitable for vessel analysis than flap in vivo model with accurate data acquirement, and the optimal observation window of flap in situ was discovered to be around 10 min after injection of QDs. Furthermore, the interlaced relationship of angiogenesis and vascular remodeling was decoded temporally that angiogenesis lasted throughout the 21 days while vascular remodeling accelerated after 14 d post-surgery. Besides, the spatial map of angiogenesis and vascular remodeling in four perforasomes were portrayed that Zone IV entered the sequential process of vascularization rapidly relying on sufficient blood supply from the LDCIA while Zone II was the latest to recover from ischemia. This work shed light on insightful understanding of spatiotemporal characteristics of vascularization by visualizing and evaluating angiogenesis and vascular remodeling simultaneously and dynamically based on a promising imaging technology, laying the groundwork for further profound investigation on the complicated process of vascularization.

Supplementary Information

The online version contains supplementary material available at https://doi.org/10.1186/s12951-025-03137-z.

Additional file 1. Figure S1. Establishment of a perforator flap transplantation mouse model. a) Bright field photograph of the mouse before surgery. b) Flap dissected from the back of the mouse with a perforator vessel preserved. c) Enlarged photograph of the dissected flap with the four perforator vessels (RLTA, LLTA, RDCIA and LDCIA) marked. d) Mouse model with the flap sutured back. Figure S2. Normalized PL intensity measured from the four perforator vessels from the origin to the end. a1-a4) Schemes of RLTA, LLTA, RDCIA and LDCIA. b1-b4) Normalized PL intensity measured from RLTA, LLTA, RDCIA and LDCIA. RLTA: right lateral thoracic artery; LLTA: left lateral thoracic artery; RDCIA: right deep circumflex iliac artery; LDCIA: left deep circumflex iliac artery. Figure S3. Average vessel diameter of the four perforator vessels and total vessels length measured in the four zones. Average vessel diameter of a1) RLTA, a2) LLTA, a3) RDCIA and a4) LDCIA. Total vessels length of b1) Zone I, b2) Zone II, b3) Zone III and b4) Zone IV. RLTA: right lateral thoracic artery; LLTA: left lateral thoracic artery; RDCIA: right deep circumflex iliac artery; LDCIA: left deep circumflex iliac artery. Figure S4. Biosafety analysis of SWIR fluorescence imaging based on QDs. a) Bright field photograph and b) SWIR fluorescence image of major organs (lung, heart, spleen, kidney and liver) harvested from the mouse model injected with QDs. c) H&E staining of major organs (lung, heart, spleen, kidney and liver) harvested from the mouse model injected with QDs compared with a control group

Additional file 2. Movie S1. Intravenous injection of the QDs through tail vein in a mouse model of perforator flap transplantation.

Additional file 3. Movie S2. Disappearance of fluorescence signals in a mouse model of perforator flap transplantation after intravenous injection of the QDs

Acknowledgements
We thank Prof. Hao Chen and his team from Shanghai Institute of Materia Medica, Chinese Academy of Sciences for providing the SWIR fluorescence imaging instrument.

Author contributions
S.F., M.C. and H.L. contributed equally to this work. J.C, S.F.and M.C. designed the study. H.L., X.Z., X.D., L.F., K.X.and S.L. performed the experiments. H.L., X.D., L.F., K.X., X.Z, S.L., F.X, D.H.and F.C.analyzed the data. S.F.and M.C. contributed to the experimental design. J.C., Y.L, M.J. and Q.X. supervised the experiment procedure. S.F., M.C., and H.L. Wrote the manuscript. J.C. revised and edited the manuscript.

Funding
This work was supported by National Key R&D Program of China (2021YFA1201303), National Natural Science Foundation of China (82072521), Shanghai Rising-Star Program (Sailing Program) (22YF1438700), Science and Technology Commission of Shanghai Municipality (23S31900700 and 23410713100), Young Elite Scientists Sponsorship Program by CAST (2023QNRC001).

Availability of data and materials
No datasets were generated or analysed during the current study.

Declarations

Ethics approval and consent to participate
All animal experiments were carried out in agreement with the guidelines approved by the Animal Care Committee of the Laboratory Animal from Fudan University.

Consent for publication
Not applicable.

Competing interests
The authors declare no competing interests.

Author details
[1]Department of Sports Medicine, Huashan Hospital, Fudan University; Sports Medicine Institute of Fudan University, Shanghai 200040, China. [2]Department of Bone and Joint Surgery, Renji Hospital, School of Medicine, Shanghai Jiao Tong University, Shanghai 200127, China. [3]Shanghai Institute of Technical Physics, Chinese Academy of Sciences, Shanghai 200083, China. [4]University of Chinese Academy of Sciences, Beijing 100049, China. [5]Wuxi Ninth People's Hospital Affiliated to Soochow University, Jiangsu 214000, China. [6]School of Mathematical Sciences, Institute of Natural Sciences, and MOE-LSC, Shanghai Jiao Tong University, Shanghai 200240, China. [7]Department of Neurosurgery, Huashan Hospital, Fudan University, Shanghai 200040, China.

Received: 31 October 2024 Accepted: 19 January 2025

References

1. Potente M, Gerhardt H, Carmeliet P. Basic and therapeutic aspects of angiogenesis. Cell. 2011;146(6):873–87. https://doi.org/10.1016/j.cell.2011.08.039.
2. Crawshaw JR, Flegg JA, Bernabeu MO, Osborne JM. Mathematical models of developmental vascular remodelling: a review. PLoS Comput Biol. 2023;19(8): e1011130. https://doi.org/10.1371/journal.pcbi.1011130.
3. Nelson JA, Kim EM, Eftakhari K, Low DW, Kovach SJ, Wu LC, et al. Late venous thrombosis in free flap breast reconstruction: strategies for salvage after this real entity. Plast Reconstr Surg. 2012;129(1):8e–15e. https://doi.org/10.1097/PRS.0b013e3182361f7f.
4. Korn C, Augustin HG. Mechanisms of vessel pruning and regression. Dev Cell. 2015;34(1):5–17. https://doi.org/10.1016/j.devcel.2015.06.004.
5. Ouarné M, Pena A, Franco CA. From remodeling to quiescence: the transformation of the vascular network. Cells Dev. 2021;168: 203735. https://doi.org/10.1016/j.cdev.2021.203735.
6. West HW, Dangas K, Antoniades C. Advances in clinical imaging of vascular inflammation a state-of-the-art review. JACC: Basic Translat Sci. 2024;9(5):710–32. https://doi.org/10.1016/j.jacbts.2023.10.007.
7. Abdelfattah U, Power HA, Song S, Min K, Suh HP, Hong JP. Algorithm for free perforator flap selection in lower extremity reconstruction based on 563 cases. Plast Reconstr Surg. 2019;144(5):1202–13. https://doi.org/10.1097/prs.0000000000006167.
8. Muntean MV, Strilciuc S, Ardelean F, Pestean C, Lacatus R, Badea AF, et al. Using dynamic infrared thermography to optimize color Doppler ultrasound mapping of cutaneous perforators. Med Ultrason. 2015;17(4):503–8. https://doi.org/10.1115/mu.2013.2066.174.dyn.
9. Nie JY, Lu LJ, Gong X, Li Q, Nie JJ. Delineating the vascular territory (perforasome) of a perforator in the lower extremity of the rabbit with four-dimensional computed tomographic angiography. Plast Reconstr Surg. 2013;131(3):565–71. https://doi.org/10.1097/PRS.0b013e31827c6e49.
10. Lee JW, Kim HK, Kim SR, Han YS, Park JH. Preoperative identification of a perforator using computed tomography angiography and metal clip marking in perforator flap reconstruction. Arch Plast Surg. 2015;42(1):78–83. https://doi.org/10.5999/aps.2015.42.1.78.
11. Azuma R, Morimoto Y, Masumoto K, Nambu M, Takikawa M, Yanagibayashi S, et al. Detection of skin perforators by indocyanine

green fluorescence nearly infrared angiography. Plast Reconstr Surg. 2008;122(4):1062–7. https://doi.org/10.1097/PRS.0b013e3181858bd2.
12. Fu Z, Zhang J, Lu Y, Wang S, Mo X, He Y, et al. Clinical applications of superb microvascular imaging in the superficial tissues and organs: a systematic review. Acad Radiol. 2021;28(5):694–703. https://doi.org/10.1016/j.acra.2020.03.032.
13. Woloszyk A, Wolint P, Becker AS, Boss A, Fath W, Tian Y, et al. Novel multimodal MRI and MicroCT imaging approach to quantify angiogenesis and 3D vascular architecture of biomaterials. Sci Rep. 2019;9(1):19474. https://doi.org/10.1038/s41598-019-55411-4.
14. Mirg S, Turner KL, Chen H, Drew PJ, Kothapalli SR. Photoacoustic imaging for microcirculation. Microcirculation. 2022;29(6–7): e12776. https://doi.org/10.1111/micc.12776.
15. Zenn MR. Fluorescent angiography. Clin Plast Surg. 2011;38(2):293–300. https://doi.org/10.1016/j.cps.2011.03.009.
16. Zhu S, Tian R, Antaris AL, Chen X, Dai H. Near-infrared-II molecular dyes for cancer imaging and surgery. Adv Mater. 2019;31(24): e1900321. https://doi.org/10.1002/adma.201900321.
17. Meng X, Pang X, Zhang K, Gong C, Yang J, Dong H, et al. Recent advances in near-infrared-II fluorescence imaging for deep-tissue molecular analysis and cancer diagnosis. Small. 2022;18(31): e2202035. https://doi.org/10.1002/smll.202202035.
18. Shi T, Huang C, Li Y, Huang F, Yin S. NIR-II phototherapy agents with aggregation-induced emission characteristics for tumor imaging and therapy. Biomaterials. 2022;285: 121535. https://doi.org/10.1016/j.biomaterials.2022.121535.
19. Li C, Chen G, Zhang Y, Wu F, Wang Q. Advanced fluorescence imaging technology in the near-infrared-II window for biomedical applications. J Am Chem Soc. 2020;142(35):14789–804. https://doi.org/10.1021/jacs.0c07022.
20. Wang ZG, Liu SL, Pang DW. Quantum dots: a promising fluorescent label for probing virus trafficking. Acc Chem Res. 2021;54(14):2991–3002. https://doi.org/10.1021/acs.accounts.1c00276.
21. Meng X, Li H, Chen Y, Sai L, Feng S, Li K, et al. In vivo precision evaluation of lymphatic function by SWIR luminescence imaging with PbS quantum dots. Adv Sci (Weinh). 2023;10(7): e2206579. https://doi.org/10.1002/advs.202206579.
22. Yang Y, Chen M, Wang P, Sai L, Chen C, Qian P, et al. Highly thermal stable RNase A@PbS/ZnS quantum dots as NIR-IIb image contrast for visualizing temporal changes of microvasculature remodeling in flap. J Nanobiotechnology. 2022;20(1):128. https://doi.org/10.1186/s12951-022-01312-0.
23. Feng S, Chen J, Wo Y, Li Y, Chen S, Zhang Y, et al. Real-time and long-time in vivo imaging in the shortwave infrared window of perforator vessels for more precise evaluation of flap perfusion. Biomaterials. 2016;103:256–64. https://doi.org/10.1016/j.biomaterials.2016.06.043.
24. Chen M, Feng S, Yang Y, Li Y, Zhang J, Chen S, et al. Tracking the in vivo spatio-temporal patterns of neovascularization via NIR-II fluorescence imaging. Nano Res. 2020;13(11):3123–9. https://doi.org/10.1007/s12274-020-2982-7.
25. Zudaire E, Gambardella L, Kurcz C, Vermeren S. A computational tool for quantitative analysis of vascular networks. PLoS ONE. 2011;6(11): e27385. https://doi.org/10.1371/journal.pone.0027385.
26. Hirata A, Mine K, Hayashi K. Contractility of temporal inverted internal limiting membrane flap after vitrectomy for macular hole. Sci Rep. 2021;11(1):20035. https://doi.org/10.1038/s41598-021-99509-0.
27. Yoon AP, Jones NF. Critical time for neovascularization/angiogenesis to allow free flap survival after delayed postoperative anastomotic compromise without surgical intervention: a review of the literature. Microsurgery. 2016;36(7):604–12. https://doi.org/10.1002/micr.30082.
28. Mao Y, Li H, Ding M, Hao X, Pan J, Tang M, et al. Comparative study of choke vessel reconstruction with single and multiple perforator-based flaps on the murine back using delayed surgery. Ann Plast Surg. 2019;82(1):93–8. https://doi.org/10.1097/sap.0000000000001637.
29. Wu ZJ, Ibrahim MM, Sergesketter AR, Schweller RM, Phillips BT, Klitzman B. The influence of topical vasodilator-induced pharmacologic delay on cutaneous flap viability and vascular remodeling. Plast Reconstr Surg. 2022;149(3):629–37. https://doi.org/10.1097/prs.0000000000008829.
30. Furtado J, Eichmann A. Vascular development, remodeling and maturation. Curr Top Dev Biol. 2024;159:344–70. https://doi.org/10.1016/bs.ctdb.2024.02.001.
31. Luo G, Zhou Z, Cao Z, Huang C, Li C, Li X, et al. M2 macrophage-derived exosomes induce angiogenesis and increase skin flap survival through HIF1AN/HIF-1α/VEGFA control. Arch Biochem Biophys. 2024;751: 109822. https://doi.org/10.1016/j.abb.2023.109822.
32. He JB, Ma XY, Li WJ, Liu YY, Lin DS. Exenatide inhibits necrosis by enhancing angiogenesis and ameliorating ischemia/reperfusion injury in a random skin flap rat model. Int Immunopharmacol. 2021;90: 107192. https://doi.org/10.1016/j.intimp.2020.107192.
33. Luo Z, Wu P, Qing L, Zhou Z, Yu F, Zhang P, et al. The hemodynamic and molecular mechanism study on the choke vessels in the multi-territory perforator flap transforming into true anastomosis. Gene. 2019;687:99–108. https://doi.org/10.1016/j.gene.2018.11.019.
34. Zhuang Y, Hu S, Wu D, Tang M, Xu DC. A novel in vivo technique for observations of choke vessels in a rat skin flap model. Plast Reconstr Surg. 2012;130(2):308–17. https://doi.org/10.1097/PRS.0b013e3182589c0e.
35. Bergeron L, Tang M, Morris SF. A review of vascular injection techniques for the study of perforator flaps. Plast Reconstr Surg. 2006;117(6):2050–7. https://doi.org/10.1097/01.prs.0000218321.36450.9b.
36. Potente M, Mäkinen T. Vascular heterogeneity and specialization in development and disease. Nat Rev Mol Cell Biol. 2017;18(8):477–94. https://doi.org/10.1038/nrm.2017.36.
37. Saint-Cyr M, Wong C, Schaverien M, Mojallal A, Rohrich RJ. The perforasome theory: vascular anatomy and clinical implications. Plast Reconstr Surg. 2009;124(5):1529–44. https://doi.org/10.1097/PRS.0b013e3181b98a6c.

Publisher's Note